DOI: 10.1002/((please add manuscript number))
Article type: Communication

Highly Efficient Perovskite-Perovskite Tandem Solar Cells Reaching 80% of the Theoretical Limit in Photovoltage

Adharsh Rajagopal[1#], Zhibin Yang[1#], Sae Byeok Jo[1], Ian L. Braly[2], Po-Wei Liang[1], Hugh W. Hillhouse[2], and Alex K.-Y. Jen[1,3]*

A. Rajagopal, Dr. Z. Yang, Dr. S. B. Jo, I. L. Braly, P.-W. Liang, Prof. H. W. Hillhouse, Prof. A. K.-Y. Jen

[1]Department of Materials Science and Engineering, University of Washington, Seattle, WA 98195, USA.

[2]Department of Chemical Engineering, Molecular Engineering and Sciences Institute, University of Washington, Seattle, Washington 98195, USA.

[3]Department of Biology and Chemistry, City University of Hong Kong, Kowloon, Hong Kong

[#]These authors contributed equally to this work.

*Corresponding author. E-mail: alexjen@cityu.edu.hk

Keywords: monolithic tandem, open-circuit voltage, hysteresis and photo stability, optical simulations, solar water splitting

Abstract: Organic-inorganic hybrid perovskite multi-junction solar cells have immense potential to realize power conversion efficiencies (PCEs) beyond the Shockley-Queisser limit of single-junction solar cells, however, they are limited by large non-ideal photovoltage loss ($V_{oc,loss}$) in small and large bandgap subcells. In this work, we have utilized an integrated approach to improve V_{oc} of subcells with optimized bandgaps and fabricated perovskite-perovskite tandem solar cells with small $V_{oc,loss}$. A fullerene variant, Indene-C_{60} bis-adduct is

used to achieve optimized interfacial contact in small bandgap (~1.2 eV) subcell that facilitates higher quasi-fermi level splitting, reduces non-radiative recombination, alleviates hysteresis instabilities, and improves V_{oc} to 0.84 V. Compositional engineering of large bandgap (~1.8 eV) perovskite is employed to realize a subcell with transparent top electrode and photo-stabilized V_{oc} of 1.22 V. The resultant monolithic perovskite-perovskite tandem solar cell shows a high V_{oc} of 1.98 V (approaching 80% of the theoretical limit) and a stabilized PCE of 18.5%. The significantly minimized non-ideal $V_{oc,loss}$ is better than the state-of-the-art silicon-perovskite tandem solar cells, which highlights prospects of using perovskite-perovskite tandems for solar energy generation. It also unlocks opportunities for water splitting using hybrid perovskites with solar-to-hydrogen (STH) efficiencies beyond 15%.

Organic-inorganic hybrid perovskites are chemically diverse, multifunctional semiconductors that have recently generated immense interest in the field of optoelectronics and photovoltaic industry.[1–7] Power conversion efficiencies (PCEs) beyond 22% have been realized for perovskite solar cells (PVSCs), which is close to single-junction Shockley-Queisser (SQ) limit.[8,9] To further improve PCE, it is highly desirable to develop all perovskite tandem solar cells, which possess merits of solution processability and low-cost, large-scale manufacturing capability inherent to hybrid perovskites. Characteristically sharp absorption onset and low open-circuit voltage loss ($V_{oc,loss}$) makes hybrid perovskites[10] ideal material for tandem application. In addition, the versatility of hybrid perovskites[3] have enabled the development of high quality photovoltaic materials over a wide-range of bandgaps (1.2-2.3 eV), which is pivotal for building all perovskite tandem solar cells.

Perovskite-perovskite tandems can be constructed by either mechanically stacking (4-terminal, 4-T) or monolithically series integrating (2-terminal, 2-T) subcells. A 4-T configuration is relatively insensitive to bandgap (E_g) matching and primarily reliant on the efficacy of individual subcells, while precise E_g matching is required in a 2-T configuration due to the need for current matching (**Figure 1**). Nevertheless, the 2-T configuration is preferred over 4-T because it has minimized parasitic absorption, higher practical efficiency, and is superior from the economic point of view.[11] In perspective to hybrid perovskites, PCE of ~36% is theoretically achievable using an optimal E_g combination of 1.2 and 1.8 eV in a 2-T configuration (**Figure 1**). Therefore, to further advance 2-T perovskite tandems is an exciting scientific challenge which will facilitate further hybrid perovskites development and lower the PV cost to facilitate technology translation.

Earlier development of 2-T tandem PVSCs were restricted by lacking of small E_g perovskites and difficulty in achieving orthogonal processability (PCE limited to <10%).[12,13] Although, thermal evaporation was employed to circumvent processing challenges, device performance was still limited (~15% PCE) due to non-optimized E_g combination (1.6 eV and 2 eV materials were used) and significant current-voltage (*J-V*) hysteresis.[14] Development of semitransparent PVSCs with sputtered ITO top electrode[15] and small E_g (~1.2 eV) Pb/Sn binary perovskites[16–19] have recently enabled construction of 2-T tandems with solution processable perovskite absorbers and optimized E_g combination (1.2 eV with 1.8 eV), resulting in a PCE of ~17%.[20] However, the performance is still limited by severe photovoltage loss ($V_{oc,loss}=E_g/q - V_{oc}$).

The highest photovoltage for monolithic 2-T tandem PVSCs with an ideal E_g combination is only ~67% of the theoretical (Shockley-Queisser) limit,[20] which is inferior to ~74% achieved in the state-of-the-art 2-T perovskite-silicon tandem (V_{oc} ~1.65 V, PCE ~23.6%)[21]

(**Table S1**). The potential of realizing high photovoltage is a distinctive advantage of such series-connected tandem architecture, however, it has not been accomplished in perovskite-perovskite tandems due to photo instability, limited V_{oc} and hysteresis of individual subcells. The theoretical limit in photovoltage for 2-T tandem is defined by the sum of $V_{oc,SQ}$ (**Figure S1**) for subcells, but the typical V_{oc} is lowered due to unavoidable SQ loss and avoidable non-ideal loss. Therefore, efforts to minimize non-ideal $V_{oc,loss}$ is critical for further advancement of 2-T tandem PVSCs.

In this work, we demonstrate a highly efficient ideal bandgap matched 2-T tandem PVSCs with minimized non-ideal $V_{oc,loss}$ via improved subcell characteristics, precise current matching and engineering of tandem construction. Mitigation of non-radiative recombination centers arising from improper interfacial energetics and poor optoelectronic characteristics of absorber materials were pivotal in reducing non-ideal $V_{oc,loss}$. Enhanced quasi-fermi level splitting (QFLS) and V_{oc} realized in both small and large E_g (~1.2 and 1.8 eV) subcells were closer to the SQ limit compared to previous works (**Figure S1**). Optical simulations were also utilized to validate current matching criterion and identify possibilities for further improving current generation in tandem architecture. Ultimately, a stable 2-T tandem cell was demonstrated with a high PCE of 18.5% under operating conditions with negligible *J-V* hysteresis. A high V_{oc} (1.98 V) was also realized, which is approaching 80% of the theoretical limit and by far the best for all perovskite monolithic tandem solar cells.

Small E_g (~1.2 eV) PVSCs. Although the early development was hindered by poor film morphologies and interfacial issues, Pb/Sn binary perovskite ($MAPb_{1-x}Sn_xI_3$) alloys have enabled the realization of the small E_g of ~1.2 eV.[16,19,22,23] A wide-range of processing techniques (solvent washing, hot casting, 2-step and anti-solvent extraction) and mixing of organic cations (methylammonium, formamidinium, cesium) were explored to attain optimal

film coverage, which eventually improved PCE of the small E_g PVSCs to 12-15%.[17,18,20,24,25] These works utilize commonly employed PEDOT:PSS and $PC_{61}BM/C_{60}$ as hole-transporting layer (HTL) and electron-transporting layer (ETL), respectively. However, compositional modification strongly perturbs frontier energy levels and results in energetic mismatch at interfaces.[25] This imposes severe limitation on device characteristics (high $V_{oc,loss}$, *J-V* hysteresis and instability under operating conditions) which are deleterious for tandem application and thus selecting appropriate interlayer is crucial.

With optimized processing conditions and additive formulation, a phase pure $MAPb_{0.5}Sn_{0.5}I_3$ film was obtained with homogenous coverage and excellent crystallinity with a E_g of ~1.22 eV (**Figure S2**). There is a significant mismatch between conduction band minimum (CBM) of $MAPb_{0.5}Sn_{0.5}I_3$ and the lowest unoccupied molecular orbital (LUMO) of C_{60}.[25] The difference in energy levels can be reduced by using an alternate fullerene variant, Indene-C_{60} bis-adduct ($IC_{60}BA$) as ETL (**Figure 2a**). To access its impact on device characteristics, p-i-n PVSCs using PEDOT:PSS as HTL and C_{60} or $IC_{60}BA$ as ETL were fabricated.

Choice of ETL strongly perturbed *J-V* characteristics of resultant devices (**Figure 2b**). Despite marginal gain in J_{sc} due to higher electron mobility of C_{60},[26] devices with C_{60} showed lower V_{oc} (0.6-0.7 V) and PCE (~10%) with apparent inverted hysteresis (higher V_{oc}, *FF* in forward scan compared to reverse scan). Conversely, much higher V_{oc} (~0.84 V) and PCE (~15%) with negligible hysteresis could be achieved using $IC_{60}BA$. Contrast in *J-V* characteristics was persistent at different scan rates ranging from 0.01 to 1 V/s (**Figure 2b** and **S3**). The difference was also evident in the stabilized maximum power output (**Figure 2c**), where device with C_{60} shows a significant decay compared to $IC_{60}BA$ which does not show any decay even after 1000 s. The observed behavior is closely tied to the electronic

nature of $MAPb_{0.5}Sn_{0.5}I_3$/ETL interface rather than any processing artifact in devices with C_{60}, demonstrated by similarity between devices with solution processed and thermally evaporated C_{60} (**Figure S4a**). Demonstration of inverted hysteresis and lower V_{oc} in devices with C_{60}:$IC_{60}BA$ (1:3) blend ETL (**Figure S4b**) further reinforces this claim. These results unambiguously demonstrate the superiority of $IC_{60}BA$ compared to C_{60} as ETL in small E_g PVSCs and establish an intimate link between interfacial properties and device characteristics. The contrast in characteristics of devices with C_{60} ETL compared to previous works[20,25,27] is related to the difference in composition and frontier energy levels of the employed Pb/Sn binary perovskite alloys.

The light intensity dependence of V_{oc} in devices was investigated to understand the factors influenced by the choice of ETL that determine hysteresis behavior and V_{oc} (**Figure 2d**). Devices with C_{60} show two distinct regions (transition from higher to lower slope as the light intensity increases), whereas devices with $IC_{60}BA$ show only a constant slope in the entire range of intensities. Observed slopes are close to previously reported values for Sn-based perovskites[18] and a similar transition of slopes has been previously observed in PVSCs with defective TiO_2/$MAPbI_3$ interface.[28] Differences in V_{oc} dependence on light intensity[29] clearly manifests that more pervasive trap-assisted recombination exists in devices with C_{60} compared to devices with $IC_{60}BA$ and is apparently an indication of defective $MAPb_{0.5}Sn_{0.5}I_3$/C_{60} interface. Sub-bandgap surface defects and interfacial fermi level pinning are likely the origin for such deleterious interface and associated consequences on device performance.[30–34] This was examined by evaluating the quasi-fermi level splitting (QFLS, $\Delta\mu_{QY}$) in $MAPb_{0.5}Sn_{0.5}I_3$ films with C_{60} and $IC_{60}BA$. QFLS enhanced with $IC_{60}BA$ compared to neat $MAPb_{0.5}Sn_{0.5}I_3$ and films with C_{60} (**Figure 2e**), evidently illustrating the significance of rational interlayer selection employed here. Higher QFLS in $MAPb_{0.5}Sn_{0.5}I_3$

(0.84±0.01 eV) realizable with $IC_{60}BA$ correlates well with device V_{oc} (0.84 V) and demonstrates improved quality of interfacial contact.

Additional transient spectroscopic studies were carried out to further pinpoint the impact of interfaces. Recent studies by Petrozza et al.[34] and Ginger et al.[35] clearly illustrate that an optimized contact should have non-quenched PL at open-circuit due to minimized non-radiative interfacial recombination. Accordingly, at open-circuit we observe that PL is dramatically quenched with addition of C_{60} to $MAPb_{0.5}Sn_{0.5}I_3$, whereas an opposite trend is observed with addition of $IC_{60}BA$ (**Figure 2f**). In fact, we observe slower PL decay and higher photoluminescence quantum yield (PLQY) with $IC_{60}BA$ compared to that of the neat $MAPb_{0.5}Sn_{0.5}I_3$ films, which highlights the dramatic reduction in non-radiative recombination alike above results (**Figure 2g**). Furthermore, femtosecond transient absorption spectroscopy[36–38] also revealed distinct beneficial characteristics of interfacial contact with $IC_{60}BA$ (**Figure 2h**).

Under same excitation fluence (0.1 μJ/cm^2), both C_{60} and $IC_{60}BA$ exhibited a similar population quenching of photo-bleaching at high energy band (PB1) corresponding to initial ultrafast charge transfer in vicinity of interfaces along with carrier cooling (**Figure S5**). However, photo-bleaching at the band edge (PB2) of $MAPb_{0.5}Sn_{0.5}I_3$ films with $IC_{60}BA$ showed drastically higher populations (**Figure 2h**) illustrating that both hot and relaxed charge carriers do not suffer from charge transfer losses at the interface during population/repopulation of perovskite films unlike interface with C_{60}. The trend is even clearer in the kinetics of PB2 and PL (**Figure S6** and **2g, i**). A slow characteristic decay time despite higher band-edge population and strong bimolecular recombination characteristics[35,39] support the formation of intimate contact between $MAPb_{0.5}Sn_{0.5}I_3$ and $IC_{60}BA$ (**Table S2**).

The intimate contact alleviates non-radiative recombination losses from intrinsic and photo-induced sub-gap defect states[34,40,41] during charge transfer process across $IC_{60}BA$, in contrast to the mis-matched $MAPb_{0.5}Sn_{0.5}I_3/C_{60}$ interface quenching charge carriers non-radiatively and hindering repopulation process at interfaces. Deleterious interface formation explains the appearance of inverted hysteresis in devices with C_{60}, where pile up charges at the corresponding interface would beneficially impact electron extraction as recently demonstrated by Tress et al.[33] The observations agree well with previously determined analogous correlations between interfacial trap sites, device hysteresis and V_{oc}.[10,30,31] Striking difference in hysteresis behavior between devices with C_{60} and $IC_{60}BA$ is therefore itself an elegant demonstration of interfaces role in $MAPb_{0.5}Sn_{0.5}I_3$ and signifies importance of $IC_{60}BA$ to realize stable devices with minimized photovoltage loss (**Figure 2b-c**).

Relatively small PLQY, faster PL decay along with population and decay behavior of PB2 illustrate dominance of non-radiative losses over beneficial impact of high C_{60} electron mobility on charge transfer at the $MAPb_{0.5}Sn_{0.5}I_3/C_{60}$ interface, which ultimately constrained device performance. With $IC_{60}BA$ we not only mitigate hysteresis related instability but also realize a remarkably high V_{oc} (0.84 V) which is ~88% of the SQ limit. Stable devices with small $V_{oc,loss}$ (~0.38 V) realized here is the lowest among reported small E_g PVSCs (**Figure S1**) and is comparable to the state-of-the-art inorganic photovoltaic technologies.[6] This provides a platform to realize high V_{oc} in 2-T tandem PVSCs.

Large E_g (~1.8 eV) PVSCs. Development of large E_g perovskites with bandgap between 1.70 to 1.75 eV (by halide mixing) has been driven by the motivation for coupling with silicon solar cell in tandem configuration.[42,43] A challenging issue in the development of large E_g perovskites is material's vulnerability to light-induced phase segregation, which tends to result in high $V_{oc,loss}$ and instability under operating conditions.[44,45] Several

approaches like enhancing grain size, mixing of FA and Cs cations, substituting Pb with Sn have been successfully utilized to alleviate adverse impact of phase segregation and realize efficient PVSCs with E_g ~1.73 eV.[42,43,46] However, the lowest E_g (~1.2 eV) perovskite requires complementary E_g of ~1.80-1.85 eV for current matching in 2-T tandem PVSCs (**Figure 1**). To realize photo-stable, efficient PVSCs based on ~1.8 eV E_g is an arduous task because phase segregation is sensitive to film composition, morphology, and processing conditions.[44,45,47] Even the state-of-the-art PVSCs based on photo-stable perovskite with ~1.8 eV E_g still suffer from huge $V_{oc,loss}$ (**Figure S1**).[20]

Methylammonium based large E_g perovskites was chosen to avoid the potential formation of deleterious non-perovskite phases and maintain processing temperatures ≤ 100°C. A E_g of ~1.8 eV was realized using $MAPb(I_{0.6}Br_{0.4})_3$ and phase segregation in this composition has been alleviated previously by engineering internal bonding environment through partial substitution of lead by tin, but suffered from low V_{oc} due to poor PLQY.[43] To overcome photo instability without compromising optoelectronic quality, we chose to engineer the lattice in an analogous manner, via partial replacement of MA by Cs.

A series of single junction PVSCs (device structure in **Figure S7a**) were fabricated to optimize the amount of Cs incorporated in $MAPb(I_{0.6}Br_{0.4})_3$. The device with 10% Cs showed the best device performance (**Figures S7b-c, f**) with high V_{oc} of 1.2 V and a PCE of 12.5% with negligible *J-V* hysteresis (**Figure 3a**). $MA_{0.9}Cs_{0.1}Pb(I_{0.6}Br_{0.4})_3$ films were phase pure (**Figure 7d**) and exhibited relatively longer lifetime (**Figure S7e**) due to improved crystallinity with Cs incorporation.[47] Moreover, striking differences were observed in photo-stability of $MAPb(I_{0.6}Br_{0.4})_3$ and $MA_{0.9}Cs_{0.1}Pb(I_{0.6}Br_{0.4})_3$ based PVSCs. With Cs incorporation, devices were photo-stable and current density at the maximum power point (MPP) was constant under continuous illumination (1 h), whereas devices without Cs showed

significant decay in less than 10 min of illumination (**Figure 3b**). This stability under operating conditions is critical for 2-T tandem, where any change in subcell behavior will impact current matching and significantly degrade tandem performance.

Optoelectronic quality and photovoltage losses in $MA_{0.9}Cs_{0.1}Pb(I_{0.6}Br_{0.4})_3$ were evaluated using time-resolved photoluminescence (TRPL) spectroscopy. Absolute PL intensity spectra and absorbance are shown in the inset of **Figure 3c** and the E_g is ~1.82 eV. A relatively stable QFLS ~1.23 eV was observed which correlates well with the device V_{oc} (**Figure 3c**). Though the V_{oc} of large E_g devices obtained here is better than that obtained from previous work[20] (**Figure S1**), a $V_{oc,loss}$ of ~0.3 V compared to SQ limit still exists. Deleterious non-radiative recombination due to material quality (PLQY <0.01%) along with mismatched energy levels (~0.35 eV) at the $NiO_x/MA_{0.9}Cs_{0.1}Pb(I_{0.6}Br_{0.4})_3$ interface (**Figure S8**) limited V_{oc} and could be improved in the future by defect passivation and development of appropriate interlayers.

To enable monolithic tandem, the top Ag electrode was replaced with sputtered ITO which transmits unabsorbed light efficiently and provides robustness for subsequent solution processing. The resultant devices performed well and showed a V_{oc} of ~1.22 V, a J_{sc} of ~12.1 mA/cm^2, a FF of ~0.69 and a PCE of ~10.1% (**Figure 3a**), analogous to Ag electrode devices discussed above. The drop in J_{sc} is reasonable considering an increased transmittance of long wavelength light through top ITO and correlates well with corresponding EQE spectra (**Figure S7c**). The device stack is unaffected during sputtering and the superior performance of semitransparent devices without compromising in V_{oc} ensures high optoelectronic quality of sputtered ITO.

2-Terminal monolithic tandem PVSCs. Selection of appropriate ICL and realization of current matching between subcells are keys for achieving effective coupling of above developed small and large E_g PVSCs to realize successful 2-T tandem cells. Accordingly, the

tandem device structure (**Figure 4a**) was designed to have sputtered ITO sandwiched between C_{60}/Bis-C_{60} and PEDOT:PSS as ICL. The energetics of ITO relative to adjoining interlayers (**Figure 4b**) along with its superior electrical conductivity ensure effective transfer of charge carriers and efficient recombination to reduce electrical losses. To assess current generation in subcells and optical losses limiting J_{sc}, transfer matrix model based optical simulations were performed. Refractive indices of perovskite absorbers and all other layers used in optical simulations are presented in **Figure 4c** and **S9**.

Figure 4d shows the variation of subcell photocurrents (J_{ph}) as a function of large E_g and small E_g layer thickness ranging from 150-450 nm and 300-600 nm, respectively. As the thickness of large E_g layer increases, the front subcell photocurrent ($J_{ph,f}$) continually increases at the expense of back subcell photocurrent ($J_{ph,b}$). A proportional increase in thickness of small E_g layer can minimize mismatch in J_{ph} arising due to this compromise. The corresponding variation in overall tandem J_{ph} determined by current-limiting subcell is shown in **Figure S10a**. The profile of $J_{ph,f}$ and $J_{ph,b}$ intersects at a certain line of thickness corresponding to the current-matched conditions among subcells in tandem configuration (**Figure 4d**). The line of current-matching along with difference in subcell photocurrents for entire range of thicknesses are portrayed via a 2D-contour plot in **Figure 4e**. The point of intersection for thickness combination used here was observed to lie right on the line corresponding to the current-matched condition. Further, the ICL ITO thickness has negligible impact on subcell photocurrent and does not significantly diverge from current matching (**Figure S10b**). A 100 nm ICL ITO was chosen and it has small parasitic absorption due to lower extinction coefficient (**Figure S9b**).

The fabrication scheme for tandem solar cells was tailored specifically to facilitate contact of ITO ICL and thus enables the possibility for examining each subcell individually

(**Figure S11**). **Figure 5a** shows the cross-section SEM image of a typical tandem cell where clear demarcation between layers are observed. The corresponding layer thicknesses and simulated optical field intensity distribution within device stack are portrayed in **Figure 5b**. With our optimized layer thicknesses, wavelength less than and greater than 700 nm are concentrated in large E_g and small E_g layers, respectively, which ensures maximized current generation in subcells.

J-V characteristics of the best performing 2-T tandem (**Figure 5c**) shows an exceptional V_{oc} of 1.98 V, a J_{sc} of 12.7 mA/cm^2, and a FF of 0.73 resulting in a remarkable PCE of 18.4%. No obvious *J-V* hysteresis was observed (**Figure S12**). The EQE of subcells (**Figure 5d**) showed excellent current matching as predicted by optical simulations and integrated currents agree well with the J_{sc} obtained from *J-V* characteristics. The reliability of PCE was further confirmed by measuring the steady-state current output at MPP (~1.55 V) which provided a stabilized efficiency of ~18.5% (**Figure 5e**). An absolute PCE improvement of ~4% is realized compared to single-junction device (**Figure 5c** and **Table 1**). When the constituent subcells were combined individually in a 4-terminal configuration, the PCE drops to 16.7% (**Figure S13**) due to increased parasitic absorption. Statistics of performance metrics for all devices studied in this work are summarized in **Figure S14**. To the best of our knowledge, 18.5% PCE obtained here is the highest performance for monolithic 2-T tandem PVSCs reported till date (**Figure 5f**).[12,14,20] Further, if an electrolyzer is coupled in series with the 2-T tandem developed here and operated at conditions close to the maximum power point (~1.55 V and 11.8 mA/cm^2), water splitting with remarkably high solar-to-hydrogen (STH) efficiencies ~15% would be realizable (details in supporting information), which is a significant improvement compared to the previous demonstration with series-connected perovskite solar cells.[48]

A large V_{oc} (~1.98 V) close to the sum of subcell *V*oc's realized for tandem cell manifests the effectiveness of rational design in our work. This is a significant improvement compared to previously reported V_{oc} (1.66 V) for similar bandgap-matched 2-T perovskite tandem.[20] Relationships between experimental V_{oc} and the various upper bounds of V_{oc} are summarized in **Figure S15**. Overall $V_{oc,loss}$ (E_{g1}/q + E_{g2}/q - V_{oc}) for the resultant 2-T tandem is substantially reduced and the non-ideal $V_{oc,loss}$ (related to interfacial energetics and absorber optoelectronic quality) is ~0.5 V which is much smaller than the previously reported non-ideal V_{oc} loss (0.7-0.8 V).[14,20] A comparison of $V_{oc,loss}$ and PCE of 2-T tandem PVSCs reported so far clearly shows that this work outperforms earlier works (**Figure 5f**). [12,14,20]

To provide broader outlook, the 2-T perovskite tandem developed here was also compared with other state-of-the-art series connected tandem cells (**Figure 5g** and **Table S1**), where PVSC is seamlessly coupled with another PV technology (OPV, CIGS and Silicon).[21,49,50] The key difference to note is the non-ideal loss, ~30% of E_g/q in case of tandems with OPV and CIGS, which ultimately limits V_{oc}. However, employment of well-established silicon PV has reduced the non-ideal loss fraction to ~21% in silicon-perovskite tandem and a record PCE of ~23.6% was achieved.[21] The 2-T perovskite tandem developed here has a non-ideal loss fraction (~17%) lower than the record silicon-perovskite tandem and the realized V_{oc} (~1.98 V) corresponds to an impressive ~80% of the theoretical limit (**Figure 5g**). It is important to note that there are several other perovskite-silicon tandems reported with different non-ideal loss fractions[51–53] and only the work with highest power conversion efficiency[21] is compared here to maintain simplicity and consistency.

With the realization of high V_{oc} and FF, the PCE of tandems are currently limited by relatively moderate J_{sc} (~13 mA/cm^2). The analysis of different aspects in light extinction and current generation in 2-T tandem cells (**Figure 5h** and **S16**) shows that small E_g subcell is the

current-limiting factor. An increase in thickness of perovskite layers will substantially improve the J_{sc} (**Figure S10a**) and a PCE of ~20-24% is certainly realizable in the near future. Further improvement in optoelectronic quality of perovskite absorbers, minimization of parasitic losses, development of appropriate interlayer and molecular strategies to dope $IC_{60}BA$ may ultimately push the J_{sc} and PCE of 2-T tandem PVSCs to even higher values.

In summary, we have successfully realized highly efficient bandgap-matched 2-T perovskite tandem solar cells by applying an integrated process, compositional, interfacial, optical, and device engineering. $IC_{60}BA$ was employed to achieve optimized interfacial contact with a small E_g (~1.2 eV) perovskite ($MAPb_{0.5}Sn_{0.5}I_3$). It shows perfect "nonquenching" at open-circuit due to reduced non-radiative recombination losses. This enables devices with negligible hysteresis and high V_{oc} (0.84 V). Devices based on the large E_g (~1.8 eV) perovskite ($MA_{0.9}Cs_{0.1}Pb(I_{0.6}Br_{0.4})_3$) with sputtered ITO as top electrode showed a high photo-stabilized V_{oc} of 1.22 V. Optical simulations were also used to ensure current matching and the resultant 2-T tandem device exhibited a very high V_{oc} (1.98 V) and PCE (18.5%). The reduced photovoltage loss (V_{oc} approaching 80% of the theoretical limit) is the lowest among all the perovskite based tandem solar cells reported so far, which demonstrates the strong potential of perovskite-perovskite tandems. With further increase in absorber thicknesses and improvement in perovskite optoelectronic quality, even higher PCEs of ~20-24% should be reachable with 2-T tandem PVSCs.

Experimental

Solution preparation: For large bandgap perovskites, $MA_{0.9}Cs_{0.1}Pb(I_{0.6}Br_{0.4})_3$ precursor solution was prepared by dissolving MAI (0.143 g), CsI (0.026 g), PbI_2 (0.184 g) and $PbBr_2$ (0.220 g) in mixed solvent (1 ml, volume ratio 3:7) of dimethyl sulphoxide (DMSO) and γ-butyrolactone (GBL) and stirred at 60 °C for 1 h. For small bandgap perovskites, $MAPb_{0.5}Sn_{0.5}I_3$ precursor solution was prepared by dissolving MAI (0.159 g), PbI_2 (0.254 g), SnI_2 (0.186 g) and SnF_2 (0.008 g) in Dimethylformamide (0.7 mL) and stirred at 60 °C for 1 h; additional DMSO (0.3 ml) was added into the above precursor just before use. For fullerene ETLs, C_{60} or $IC_{60}BA$ (15 mg/mL) was dissolved in dichlorobenzene and stirred at 80 °C for 2 h. For fullerene surfactant, Bis-C_{60} (2 mg/mL) in isopropyl alcohol was dissolved using sonication (typically 1 h). For NiO_x, precursor solution was prepared by dissolving Nickel (II) acetate tetrahydrate (124.4 mg) in ethanol (5 mL) and ethanolamine (30 μL) was added to it; the mixture was stirred at 60 °C for 2 h. PEDOT:PSS (Baytron PVP AI 4083) solution was allowed to reach room temperature before usage. All solutions were filtered with 0.22 μm PVDF filters before spin coating.

Device fabrication: ITO glass substrates were initially masked using Kapton tape as per the required pattern (**Figure S11**); then zinc powder was applied on the substrates which were subsequently dipped into a beaker with concentrated hydrochloric acid for 10 s and then completely washed with water. Afterwards, sequential steps of ultrasonication for 10 min in detergent, deionized water, acetone, and isopropanol alcohol was used to clean ITO glass. Cleaned ITO glass substrates were subjected to UV ozone treatment (10 min) before start of device fabrication. NiO_x precursor was spin coated onto the clean ITO glass at 3000 rpm for 60 s and annealed at 400 ^oC for 1 h in air. After this step, substrates were transferred into N_2-filled gloveboxes. $MA_{0.9}Cs_{0.1}Pb(I_{0.6}Br_{0.4})_3$ precursor solution was spin coated onto the

substrate using 2-step spin program (1000 rpm for 15 s and 4000 rpm for 45 s); during the last 20-10 s of the second spin-coating step, toluene (0.7 ml) was dropped onto the spinning substrate and the substrates were annealed at 100 ^{o}C for 10 min using a hot plate. Subsequently, C_{60} was evaporated onto the perovskite films with a steady deposition rate (~0.2 Å/s). Then, Bis-C_{60} solution was spin coated onto at 3000 rpm for 60 s. At this stage, substrates were removed from glovebox for ITO sputtering. Around 100 nm ITO was deposited using a Lesker Sputter system (DC based magnetron sputtering) with low power (150 W) under 3 mTorr of Ar. Immediately, PEDOT:PSS solution was spin-coated on the sputtered ITO at 5000 rpm for 30 s and annealed at 100 °C for 10 min in ambient. Then substrates were transferred into glovebox again for device completion. $MAPb_{0.5}Sn_{0.5}I_3$ precursor solution was dropped on PEDOT:PSS and spin-coated at 5000 rpm for 30 s in glove box; toluene (0.7 mL) was quickly dropped onto the spinning substrate after 10 s elapse. The resulting perovskite films were annealed at 70 °C for 5 min. Subsequently, $IC_{60}BA$ or C_{60} solution was spin coated using 1500 rpm for 55 s and 4000 rpm for 5 s followed by annealing at 70 °C for 5 min. Then, Bis-C_{60} surfactant solution was spin coated on top at 3000 rpm for 60 s. Finally, a 150 nm thick silver (Ag) electrode was evaporated under high vacuum (<1×10^{-6} Torr) through a shadow mask (14 mm^2). The entire fabrication process and electrode design for tandem cells are illustrated in detail in **Figure S11**. Single junction solar cells were fabricated as per device structure using the similar procedure. All single junction and tandem solar cells were characterized by applying a shadow mask with an aperture area of 10 mm^2.

Photovoltaic characterization: Large bandgap PVSCs were tested using Class A solar simulator (Solar light 16S-300) inside glovebox, whereas small bandgap and 2-T tandem PVSCs were tested using Class AAA solar simulator (OAI TriSol) in ambient without encapsulation. To account for spectral mismatch factor, solar simulator was calibrated to

match the integrated current calculated from corresponding EQE. A calibrated reference silicon photodiode was used to measure light intensities. *J-V* scans were measured using Keithley 2400 Source Meter at different scan rates, by varying delay times at constant step size (0.01 V); delay times of 10, 100 and 1000 ms correspond to scan rates 1, 0.1 and 0.01 V/s respectively. Typical forward *J-V* scans (short circuit, SC → open circuit, OC) measured at 1 V/s were used to calculate solar cell performance metrics, unless specified. Hysteresis characteristics were measured using an uninterrupted sequence of forward and reverse scans (SC→OC→SC). Stabilized PCE were determined using steady-state current measurements at an applied voltage corresponding to maximum power point without encapsulation. Light intensity dependent measurements were performed using a set of neutral density filters; *J-V* characteristics were measured under eight different intensities ranging between 0.5 to 100 mW/cm^2. The linear fits of data had high degree of accuracy, with R-squared values generally > 0.98. Analysis and interpretation of illumination intensity dependent *J-V* data are in accordance to literature.[18,28,29] For all measurements under illumination, the shutter was opened just before measurement and no intentional light or electrical bias soaking was used. EQE measurements were performed using a setup consisting of xenon lamp (Oriel, 450W) as light source, monochromator (Newport Cornerstone 130), optical chopper, lock-in amplifier (Stanford Research Corp SR830), and a NIST-certified Si-photodiode (Thorlabs FDS 100-CAL) for calibration. The fluctuation of xenon arc lamp source was within 5% during the entire period of measurements. For tandem solar cells, EQE spectra were measured by contacting the middle electrode (sputtered ITO) with bottom (ITO) and top (Ag) electrodes respectively to measure front and back subcells individually. EQE spectra were integrated over AM 1.5G photon-flux to attain photocurrent density. All EQE measurements were carried out in ambient without any device encapsulation.

Additional experimental details including materials, thin-film characterization, transient absorption spectroscopy, photoluminescence measurements, PL decay modelling, quasi-fermi level splitting calculations, optical simulations, and efficiency simulation for tandem solar cells are provided in supporting information.

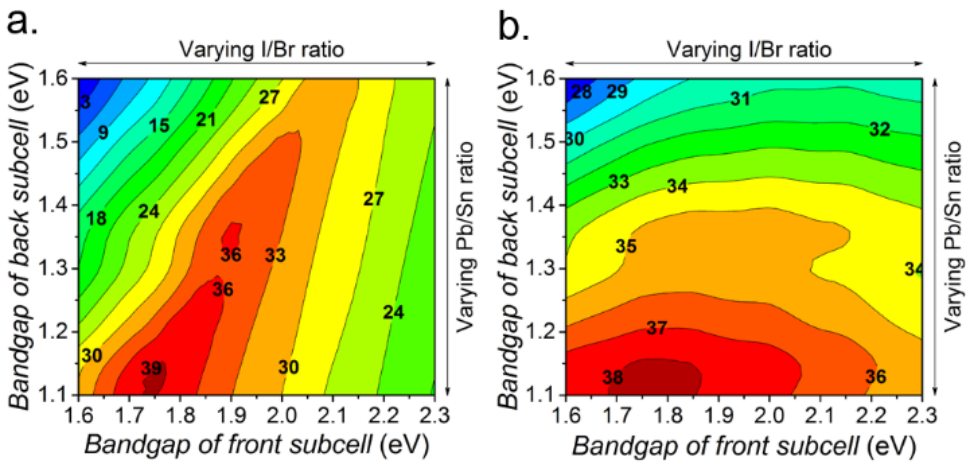

Figure 1. Efficiency limits for perovskite-perovskite tandem solar cells. a, 2-terminal and b, 4-terminal tandem configuration. Contour lines and corresponding power conversion efficiency (%) are depicted.

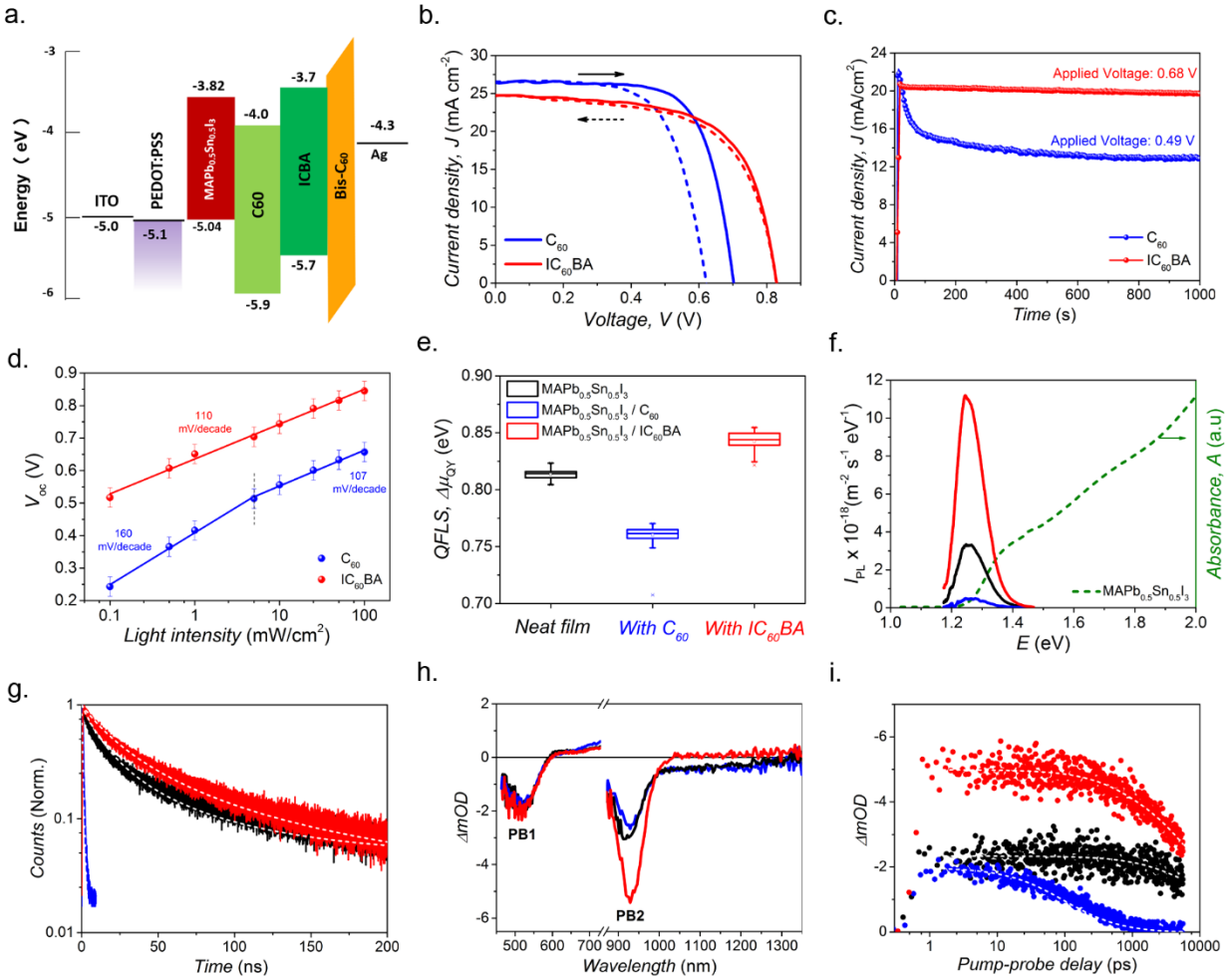

Figure 2. Photovoltaic and optoelectronic characteristics of small bandgap (~1.2 eV) perovskites. a-d, Energy level diagram (a), Typical *J-V* characteristics (b), steady-state current under AM1.5 illumination at an applied voltage corresponding to MPP (c), and light intensity dependence of V_{oc} with corresponding slopes obtained by linear fits (d) for $MAPb_{0.5}Sn_{0.5}I_3$ PVSCs with C_{60} and $IC_{60}BA$ ETLs. e-g, Quasi-fermi level splitting values (e), photoluminescence spectra (f), transient photoluminescence (g), transient absorption spectra showing two major photo-bleaching signals (PB1 and PB2) at pump-probe delay of 2 ps (h), and kinetics of band edge photo-bleaching (i) for neat $MAPb_{0.5}Sn_{0.5}I_3$, $MAPb_{0.5}Sn_{0.5}I_3$ / C_{60} and $MAPb_{0.5}Sn_{0.5}I_3$ / $IC_{60}BA$ films. Box and whisker plots in (e) show spatial average statistics where boxes are 25-75%, whiskers correspond to 1.5 interquartile range and inner line is median.

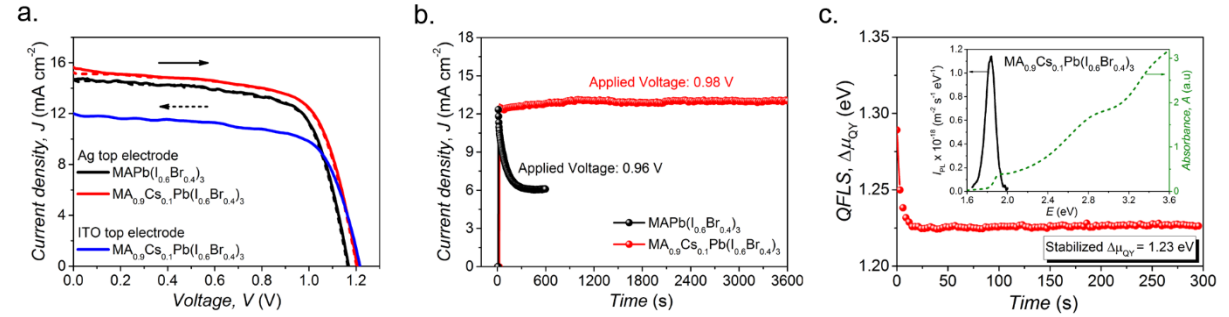

Figure 3. Photovoltaic and optoelectronic characteristics of large bandgap (~1.8 eV) perovskites. a-b, Typical J-V characteristics (a) and steady-state current under AM1.5 illumination at an applied voltage corresponding to MPP (b) of $MAPb(I_{0.6}Br_{0.4})_3$ and $MA_{0.9}Cs_{0.1}Pb(I_{0.6}Br_{0.4})_3$ PVSCs. c, Stabilized Quasi-fermi level splitting of $MA_{0.9}Cs_{0.1}Pb(I_{0.6}Br_{0.4})_3$ with initial PL spectra and absorbance shown in figure inset.

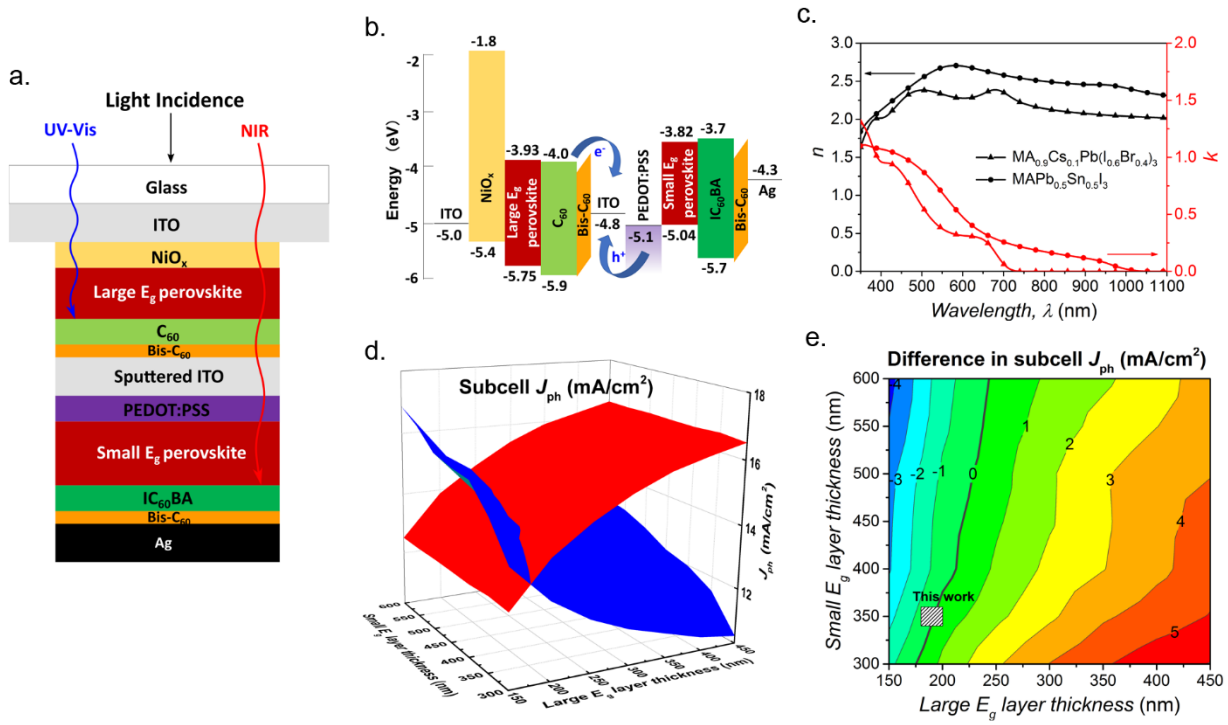

Figure 4. Energy level diagram and optical simulation of perovskite-perovskite tandem solar cells. a-b, Device structure (a), and energy level diagram (b) of 2-T tandem solar cell developed here. c, Refractive indices of small and large bandgap perovskite absorbers. d, Variation of front (red) and back (blue) subcell photocurrents (J_{ph}) as a function of large E_g and small E_g layer thicknesses. e, Corresponding difference in subcell photocurrent ($J_{ph,f}$ - $J_{ph,b}$), where contour line representing $J_{ph,f}$ - $J_{ph,b}$ = 0 (ideal current matching) is highlighted and region corresponding to thickness combination used in this work (190±10 nm and 350±10 nm) is marked.

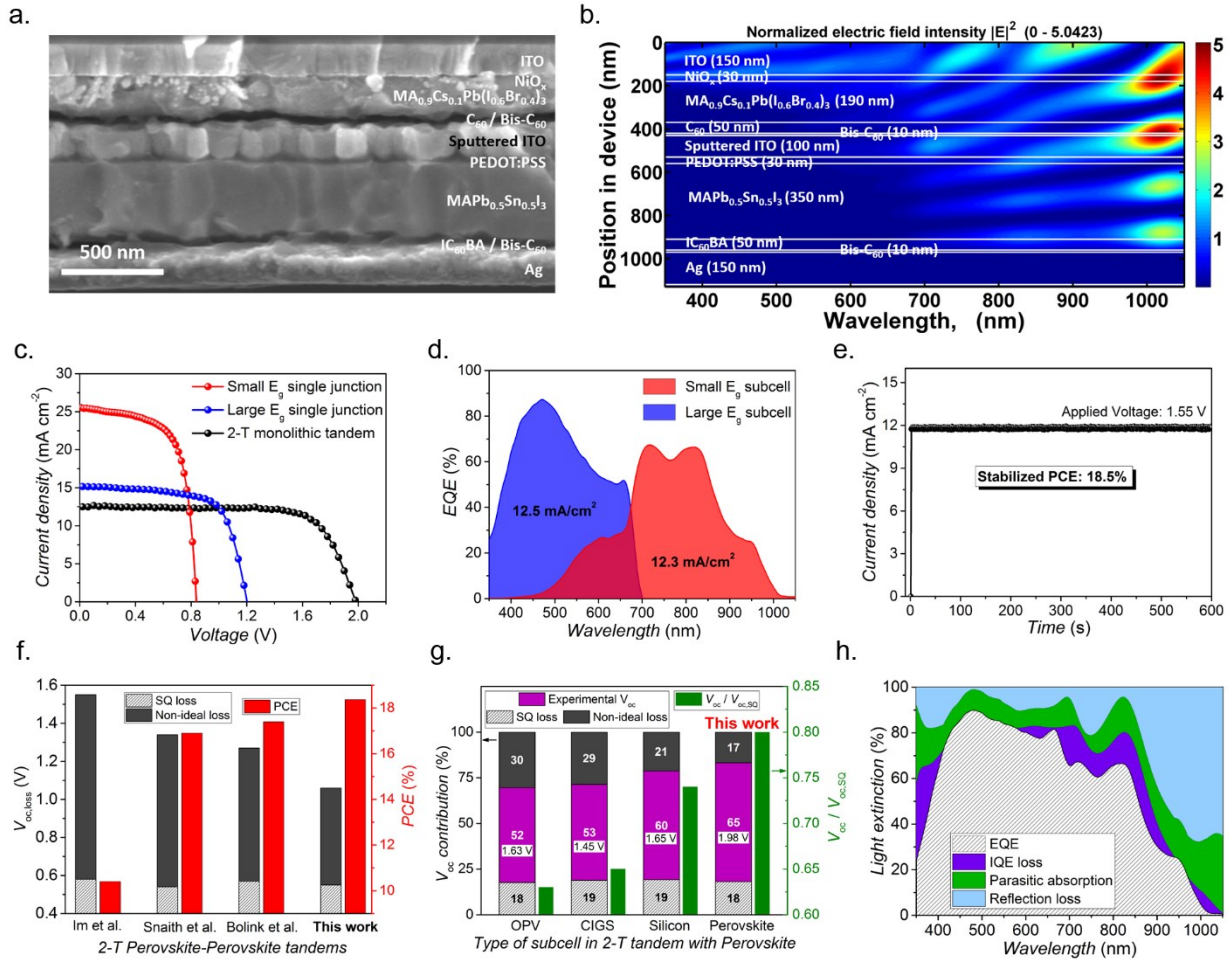

Figure 5. Photovoltaic characteristics and analysis of 2-terminal perovskite tandem solar cells. a, Cross-section SEM of a characteristic device. b, Simulated electric field intensity distribution within a tandem stack. c, Typical *J-V* characteristics of 2-terminal tandem solar cell along with that of the small and large bandgap single junction solar cells with Ag electrode. d, EQE spectra of individual subcells in 2-terminal monolithic tandem. e, Steady-state current under AM1.5 illumination at an applied voltage corresponding to MPP of tandem solar cells. f, Comparison of $V_{oc,loss}$ and PCE of perovskite-perovskite tandem developed here in perspective to literature.[13,14,20] g, Fractional contribution of V_{oc} and associated losses with respect to bandgap for different state-of-art tandem solar cells, where perovskite is monolithically integrated with other photovoltaic technologies.[21,49,50] h, Contribution of different factors (EQE, IQE loss, parasitic absorption, reflection) for light extinction in tandem solar cell developed here

Table 1. Performance metrics for single junction and 2-T perovskite-perovskite tandem solar cells.

	E_g [eV]	$\Delta\mu_{QY,Max}$ [a)] [eV]	V_{oc} [V]	J_{sc} [mA/cm^2]	FF	PCE [b)] [%]	S-PCE [c)] [%]	V_{oc}/V_{oc}^{SQ}
Small bandgap single junction	1.22	0.85	0.84	25.5	0.67	14.4	13.9	0.88
Large bandgap single junction	1.82	1.23	1.20	15.1	0.69	12.5	12.8	0.80
2-T monolithic tandem			**1.98**	**12.7**	**0.73**	**18.4**	**18.5**	**0.80** [d)]

[a)]Corresponds to stabilized maximum value; [b)]PCE obtained from forward *J-V* scan; [c)]PCE obtained from steady-state current response of the device maintained at voltage corresponding to maximum power point under AM1.5 illumination; [d)]V_{oc}^{SQ} for tandem obtained by adding SQ limit of subcells.

Supporting Information
Supporting Information is available from the Wiley Online Library or from the author.

Acknowledgements
This work was supported by the National Science Foundation (DMR-1608279), the Office of Naval Research (N00014-17-1-2260), the Asian Office of Aerospace R&D (FA2386-15-1-4106), and the Department of Energy SunShot (DE-EE 0006710). Part of this work was conducted at UW NNCI Washington Nanofabrication Facility and Molecular Analysis Facility at University of Washington. The authors thank Francis Lin for material synthesis, Ting Zhao for help with cross-section SEM imaging and Spencer T. Williams for critical evaluation of the manuscript during revision.

A.R. and Z.Y. contributed equally to this work. A.R. and Z.Y. conceived the overall work, fabricated and characterized all solar cells. P.-W.L. assisted in optimization of small bandgap subcells. A.R. performed optical simulations. S.-B.J. performed transient spectroscopic studies (TAS, TrPL). I.B. carried out TRPL measurements to estimate QFLS. A.R. wrote the manuscript and all co-authors contributed to their corresponding sections. All authors discussed results and reviewed the final manuscript. A.K.-Y.J. led the entire project.

Received: ((will be filled in by the editorial staff))
Revised: ((will be filled in by the editorial staff))
Published online: ((will be filled in by the editorial staff))

References

[1] W. Li, Z. Wang, F. Deschler, S. Gao, R. H. Friend, A. K. Cheetham, *Nat. Rev. Mater.* **2017**, 16099.
[2] B. Saparov, D. B. Mitzi, *Chem. Rev.* **2016**, *116*, 4558.
[3] T. M. Brenner, D. A. Egger, L. Kronik, G. Hodes, D. Cahen, *Nat. Rev. Mater.* **2016**, *1*, 15007.
[4] W. Zhang, G. E. Eperon, H. J. Snaith, *Nat. Energy* **2016**, *1*, 16048.
[5] B. R. Sutherland, E. H. Sargent, *Nat. Photonics* **2016**, *10*, 295.
[6] A. Polman, M. Knight, E. C. Garnett, B. Ehrler, W. C. Sinke, *Science.* **2016**, *352*, aad4424.
[7] J.-P. Correa-Baena, A. Abate, M. Saliba, W. Tress, T. Jesper Jacobsson, M. Grätzel, A. Hagfeldt, *Energy Environ. Sci.* **2017**, *10*, 710.
[8] Nrel.gov, "National Renewable Energy Laboratory," can be found under https://www.nrel.gov/pv/assets/images/efficiency-chart.png, **2017**.
[9] M. A. Green, K. Emery, Y. Hishikawa, W. Warta, E. D. Dunlop, D. H. Levi, A. W. Y. Ho-Baillie, *Prog. Photovoltaics Res. Appl.* **2017**, *25*, 3.
[10] J. Yao, T. Kirchartz, M. S. Vezie, M. A. Faist, W. Gong, Z. He, H. Wu, J. Troughton, T. Watson, D. Bryant, J. Nelson, *Phys. Rev. Appl.* **2015**, *4*, 14020.
[11] C. D. Bailie, M. D. McGehee, *MRS Bull.* **2015**, *40*, 681.
[12] J. H. Heo, S. H. Im, *Adv. Mater.* **2016**, *28*, 5121.
[13] F. Jiang, T. Liu, B. Luo, J. Tong, F. Qin, S. Xiong, Z. Li, Y. Zhou, *J. Mater. Chem. A* **2016**, *4*, 1208.
[14] D. Forgács, L. Gil-Escrig, D. Pérez-Del-Rey, C. Momblona, J. Werner, B. Niesen, C. Ballif, M. Sessolo, H. J. Bolink, *Adv. Energy Mater.* **2016**, 1602121.
[15] K. A. Bush, C. D. Bailie, Y. Chen, A. R. Bowring, W. Wang, W. Ma, T. Leijtens, F. Moghadam, M. D. McGehee, *Adv. Mater.* **2016**, *28*, 3937.
[16] F. Hao, C. C. Stoumpos, R. P. H. Chang, M. G. Kanatzidis, *J. Am. Chem. Soc.* **2014**, *136*, 8094.
[17] W. Liao, D. Zhao, Y. Yu, N. Shrestha, K. Ghimire, C. R. Grice, C. Wang, Y. Xiao, A. J. Cimaroli, R. J. Ellingson, N. J. Podraza, K. Zhu, R.-G. Xiong, Y. Yan, *J. Am. Chem. Soc.* **2016**, *138*, 12360.
[18] B. Zhao, M. Abdi-Jalebi, M. Tabachnyk, H. Glass, V. S. Kamboj, W. Nie, A. J. Pearson, Y. Puttisong, K. C. Gödel, H. E. Beere, D. A. Ritchie, A. D. Mohite, S. E. Dutton, R. H. Friend, A. Sadhanala, *Adv. Mater.* **2017**, *29*, 1604744.
[19] F. Hao, C. C. Stoumpos, P. Guo, N. Zhou, T. J. Marks, R. P. H. Chang, M. G. Kanatzidis, *J. Am. Chem. Soc.* **2015**, *137*, 11445.
[20] G. E. Eperon, T. Leijtens, K. A. Bush, R. Prasanna, T. Green, J. T.-W. Wang, D. P. McMeekin, G. Volonakis, R. L. Milot, R. May, A. Palmstrom, D. J. Slotcavage, R. A. Belisle, J. B. Patel, E. S. Parrott, R. J. Sutton, W. Ma, F. Moghadam, B. Conings, A. Babayigit, H.-G. Boyen, S. Bent, F. Giustino, L. M. Herz, M. B. Johnston, M. D. McGehee, H. J. Snaith, *Science.* **2016**, *354*, 861.
[21] K. A. Bush, A. F. Palmstrom, Z. (Jason) Yu, M. Boccard, R. Cheacharoen, J. P. Mailoa, D. P. McMeekin, R. L. Z. Hoye, C. D. Bailie, T. Leijtens, I. M. Peters, M. C. Minichetti, N. Rolston, R. Prasanna, S. Sofia, D. Harwood, W. Ma, F. Moghadam, H. J. Snaith, T. Buonassisi, Z. C. Holman, S. F. Bent, M. D. McGehee, *Nat. Energy* **2017**, *2*, 17009.
[22] N. K. Noel, S. D. Stranks, A. Abate, C. Wehrenfennig, S. Guarnera, A. Haghighirad, A. Sadhanala, G. E. Eperon, S. K. Pathak, M. B. Johnston, A. Petrozza, L. M. Herz, H.

J. Snaith, *Energy Environ. Sci.* **2014**, *7*, 3061.
[23] J. Im, C. C. Stoumpos, H. Jin, A. J. Freeman, M. G. Kanatzidis, *J. Phys. Chem. Lett.* **2015**, *6*, 3503.
[24] Y. Li, W. Sun, W. Yan, S. Ye, H. Rao, H. Peng, Z. Zhao, Z. Bian, Z. Liu, H. Zhou, C. Huang, *Adv. Energy Mater.* **2016**, *6*, 1601353.
[25] Z. Yang, A. Rajagopal, C. Chueh, S. B. Jo, B. Liu, T. Zhao, A. K.-Y. Jen, *Adv. Mater.* **2016**, *28*, 8990.
[26] P.-W. Liang, C.-C. Chueh, S. T. Williams, A. K.-Y. Jen, *Adv. Energy Mater.* **2015**, *5*, 1402321.
[27] D. Zhao, Y. Yu, C. Wang, W. Liao, N. Shrestha, C. R. Grice, A. J. Cimaroli, L. Guan, R. J. Ellingson, K. Zhu, X. Zhao, R.-G. Xiong, Y. Yan, *Nat. Energy* **2017**, *2*, 17018.
[28] L. Gouda, R. Gottesman, A. Ginsburg, D. A. Keller, E. Haltzi, J. Hu, S. Tirosh, A. Y. Anderson, A. Zaban, P. P. Boix, *J. Phys. Chem. Lett.* **2015**, *6*, 4640.
[29] L. Schmidt-Mende, J. Weickert, *Organic and Hybrid Solar Cells: An Introduction*, Walter De Gruyter GmbH, Berlin, Germany, **2016**.
[30] S. van Reenen, M. Kemerink, H. J. Snaith, *J. Phys. Chem. Lett.* **2015**, *6*, 3808.
[31] D. W. Miller, G. E. Eperon, E. T. Roe, C. W. Warren, H. J. Snaith, M. C. Lonergan, *Appl. Phys. Lett.* **2016**, *109*, 153902.
[32] S. Chen, Y. Hou, H. Chen, M. Richter, F. Guo, S. Kahmann, X. Tang, T. Stubhan, H. Zhang, N. Li, N. Gasparini, C. O. R. Quiroz, L. S. Khanzada, G. J. Matt, A. Osvet, C. J. Brabec, *Adv. Energy Mater.* **2016**, *6*, 1600132.
[33] W. Tress, J. P. Correa Baena, M. Saliba, A. Abate, M. Graetzel, *Adv. Energy Mater.* **2016**, *6*, 1600396.
[34] T. Leijtens, G. E. Eperon, A. J. Barker, G. Grancini, W. Zhang, J. M. Ball, A. R. S. Kandada, H. J. Snaith, A. Petrozza, *Energy Environ. Sci.* **2016**, *9*, 3472.
[35] G. E. Eperon, D. Moerman, D. S. Ginger, *ACS Nano* **2016**, *10*, 10258.
[36] J. S. Manser, P. V Kamat, *Nat. Photonics* **2014**, *8*, 737.
[37] T. C. Sum, N. Mathews, G. Xing, S. S. Lim, W. K. Chong, D. Giovanni, H. A. Dewi, *Acc. Chem. Res.* **2016**, *49*, 294.
[38] G. Xing, N. Mathews, S. Sun, S. S. Lim, Y. M. Lam, M. Gratzel, S. Mhaisalkar, T. C. Sum, *Science.* **2013**, *342*, 344.
[39] L. Ma, F. Hao, C. C. Stoumpos, B. T. Phelan, M. R. Wasielewski, M. G. Kanatzidis, *J. Am. Chem. Soc.* **2016**, *138*, 14750.
[40] E. S. Parrott, R. L. Milot, T. Stergiopoulos, H. J. Snaith, M. B. Johnston, L. M. Herz, *J. Phys. Chem. Lett.* **2016**, *7*, 1321.
[41] S. G. Motti, M. Gandini, A. J. Barker, J. M. Ball, A. R. Srimath Kandada, A. Petrozza, *ACS Energy Lett.* **2016**, *1*, 726.
[42] D. P. McMeekin, G. Sadoughi, W. Rehman, G. E. Eperon, M. Saliba, M. T. Horantner, A. Haghighirad, N. Sakai, L. Korte, B. Rech, M. B. Johnston, L. M. Herz, H. J. Snaith, *Science.* **2016**, *351*, 151.
[43] Z. Yang, A. Rajagopal, S. B. Jo, C.-C. Chueh, S. Williams, C.-C. Huang, J. K. Katahara, H. W. Hillhouse, A. K.-Y. Jen, *Nano Lett.* **2016**, *16*, 7739.
[44] D. J. Slotcavage, H. I. Karunadasa, M. D. McGehee, *ACS Energy Lett.* **2016**, *1*, 1199.
[45] I. L. Braly, H. W. Hillhouse, *J. Phys. Chem. C* **2016**, *120*, 893.
[46] M. Hu, C. Bi, Y. Yuan, Y. Bai, J. Huang, *Adv. Sci.* **2016**, *3*, 1500301.
[47] W. Rehman, D. P. McMeekin, J. B. Patel, R. L. Milot, M. B. Johnston, H. J. Snaith, L. M. Herz, *Energy Environ. Sci.* **2017**, *10*, 361.
[48] J. Luo, J.-H. Im, M. T. Mayer, M. Schreier, M. K. Nazeeruddin, N.-G. Park, S. D. Tilley, H. J. Fan, M. Gratzel, Science. 2014, 345, 1593.

[49] Y. Liu, L. A. Renna, M. Bag, Z. A. Page, P. Kim, J. Choi, T. Emrick, D. Venkataraman, T. P. Russell, *ACS Appl. Mater. Interfaces* **2016**, *8*, 7070.
[50] T. Todorov, T. Gershon, O. Gunawan, Y. S. Lee, C. Sturdevant, L.-Y. Chang, S. Guha, *Adv. Energy Mater.* **2015**, *5*, 1500799.
[51] S. Albrecht, M. Saliba, J. P. Correa Baena, F. Lang, L. Kegelmann, M. Mews, L. Steier, A. Abate, J. Rappich, L. Korte, R. Schlatmann, M. K. Nazeeruddin, A. Hagfeldt, M. Grätzel, B. Rech, *Energy Environ. Sci.* **2016**, *9*, 81.
[52] J. Werner, C.-H. Weng, A. Walter, L. Fesquet, J. P. Seif, S. De Wolf, B. Niesen, C. Ballif, *J. Phys. Chem. Lett.* **2016**, *7*, 161.
[53] J. Werner, L. Barraud, A. Walter, M. Bräuninger, F. Sahli, D. Sacchetto, N. Tétreault, B. Paviet-Salomon, S.-J. Moon, C. Allebé, M. Despeisse, S. Nicolay, S. De Wolf, B. Niesen, C. Ballif, *ACS Energy Lett.* **2016**, *1*, 474.

High V_{oc} (1.98 V) and PCE (18.5%) is realized in an ideal bandgap-matched two-terminal perovskite-perovskite tandem solar cells via an integrated approach to minimize the non-ideal photovoltage loss. Fullerene variant, Indene-C_{60} bis-adduct is used to achieve optimized interfacial contact and alleviate hysteresis instabilities in small bandgap subcell. Compositional engineering is employed to realize higher photo-stabilized V_{oc} in large bandgap subcell.

Keywords: monolithic tandem, open-circuit voltage, hysteresis, photo stability, optical simulations

Adharsh Rajagopal[1#], Zhibin Yang[1#], Sae Byeok Jo[1], Ian L. Braly[2], Po-Wei Liang[1], Hugh W. Hillhouse[2] and Alex K.-Y. Jen[1,3]*

Highly Efficient Perovskite-Perovskite Tandem Solar Cells Reaching 80% of the Theoretical Limit in Photovoltage